Acoustic and In-situ Observations of Deep Seafloor Hydrothermal Discharge: an OOI Cabled Array ASHES Vent Field Case Study

Guangyu Xu[1], Karen Bemis[2], Darrell Jackson[1], Anatoliy Ivakin[1]

[1]Applied Physics Laboratory, University of Washington.

[2]Department of Marine and Coastal Sciences, Rutgers, The State University of New Jersey

Corresponding author: Guangyu Xu (guangyux@uw.edu)

Key Points:

An observatory imaging sonar provides time-series observations of hydrothermal flows in both focused and diffuse forms at ASHES.

Acoustic imaging of focused discharge shows plume bending due to ambient currents and potentially sporadic venting at the source.

Bottom currents modulate the temporal variations of diffuse flows.

Abstract

The Cabled Observatory Vent Imaging Sonar (COVIS) was installed on the Ocean Observatories Initiative's Cabled Array observatory at ASHES hydrothermal vent field on Axial Seamount in July 2018. The acoustic backscatter data recorded by COVIS, in conjunction with in-situ temperature measurements, are used to investigate the temporal and spatial variations of hydrothermal discharge within ASHES. Specifically, sonar data processing generates three-dimensional backscatter images of the buoyant plumes above major sulfide structures and two-dimensional maps of diffuse hydrothermal sources within COVIS's field-of-view. The backscatter images show drastic changes of plume appearance and behavior that potentially reflect episodic variabilities of vent fluid composition and/or outflow fluxes. The diffuse-flow maps show that the areal extent of hydrothermal discharge on the seafloor varies significantly with time, which is largely driven by bottom currents and potentially tidal loading. These findings demonstrate COVIS's ability to quantitatively monitor hydrothermal discharge with sufficient spatial and temporal coverage to provide the research community with key observational data for studying the linkage of hydrothermal activity with oceanic and geological processes during the dynamic period leading up to the next eruption of Axial Seamount.

1 Introduction

Along mid-ocean ridges and atop seamounts, geothermally heated and chemically altered seawater exits near the seafloor as discharge of hydrothermal fluids that transfer considerable amounts of heat and chemicals from the earth's interior to the overlying ocean. Within a vent field, hydrothermal venting often occurs in a variety of settings, ranging from focused flows (i.e., plumes) issuing from individual vents (e.g., black smokers) to diffuse flows from the sides of sulfide mounds, isolated cracks, lava tubes, and areas of permeable seafloor. Historically,

observations of seafloor venting primarily rely on 1) in-situ measurements of venting temperature and flow rate at discrete locations and 2) mapping of the spatial extent of venting using biological cover and/or geochemical precipitates seen in seafloor images as discharge indicators. More recently, a new vent detection and mapping technique was developed, which uses a structured light laser sensor mounted on a remotely operated vehicle (ROV) to detect venting from the distortion of laser beams passing through the heated fluids coming out of hydrothermal sources (Smart et al., 2017). Although in-situ measurements have provided time series of venting properties at discrete locations and mapping has yielded snapshots of discharge over surveyed areas, systematically monitoring hydrothermal venting over sufficient space and time has remained a challenge.

The temperature fluctuations within hydrothermal fluids can scatter and distort sound waves (Xu et al., 2011; 2017), which makes underwater acoustics a natural tool for detecting and monitoring seafloor venting. Multibeam sonar observations began nearly three decades ago as an imaging tool used to provide snapshots of hydrothermal plumes issuing from focused sources (Palmer et al., 1986; Rona et al., 1991). In recent years, following the development of the Cabled Observatory Vent Imaging Sonar (COVIS), methods have been developed to obtain quantitative information of hydrothermal venting (Bemis et al., 2015). The previous deployment of COVIS at the Endeavour node of the NEPTUNE observatory operated by Ocean Networks Canada (ONC) provided an unprecedented multi-year time series of flow rate and heat flux of the focused venting on the Grotto mound (Xu et al., 2013; 2014). Subsequently, an inversion method has been developed to estimate the temperature variation associated with the diffuse flows on and near Grotto (Jackson et al., 2017). COVIS was recovered from the Endeavour site in the summer of 2015, finishing a 5-year operation since 2010.

On July 29th, 2018, COVIS was successfully installed on the Ocean Observatories Initiative's Cabled Array (OOI-CA) observatory (Kelley et al., 2014) at ASHES vent field on Axial Seamount in the Northeast Pacific. In this study, we combine the acoustic data recorded in the initial two months following the installation with in-situ measurements to investigate the spatial and temporal variabilities of seafloor venting within ASHES. Section 2 introduces the geological setting of ASHES vent field and the past observations of its local hydrothermal activity. Section 3 introduces the configuration of COVIS, its acoustic data collection and processing procedures, and associated in-situ data collection. Section 4 gives an overview of the acoustic data products and the comparison between acoustic and in-situ observations. Section 5 interprets the acoustic observations with a focus on the response of hydrothermal venting at ASHES to ocean tides and bottom currents. Section 6 offers conclusions and suggestions for future work.

2 ASHES Hydrothermal Vent Field

ASHES hydrothermal vent field is located on Axial Seamount on the Juan de Fuca Ridge in the Northeast Pacific (Figure 1a). Axial, a hot-spot volcano located on the spreading axis, has erupted recently in 1998, 2011, and 2015, making it the most volcanically active site on the Juan de Fuca Ridge (Kelley et al., 2014; Chadwick et al., 2010, 2016; Wilcock et al., 2016). Axial is also a bull's-eye study site of the OOI-CA seafloor observatory (Kelley et al., 2014). ASHES hydrothermal vent field is in the southwest corner of Axial's horseshoe shaped caldera (Figure 1a). The most vigorous venting at ASHES occurs within and around a nearly circular depression ~60 m wide and 1-2 m deep at ~100 m east of the western caldera wall (Hammond et al., 1990;

Embly et al, 1990), which is the focus of this study (Figure 1b). This northern portion of the ASHES vent field is also an area of low magnetization and may be centered over a significant upflow zone of the hydrothermal system (Tontini et al., 2016).

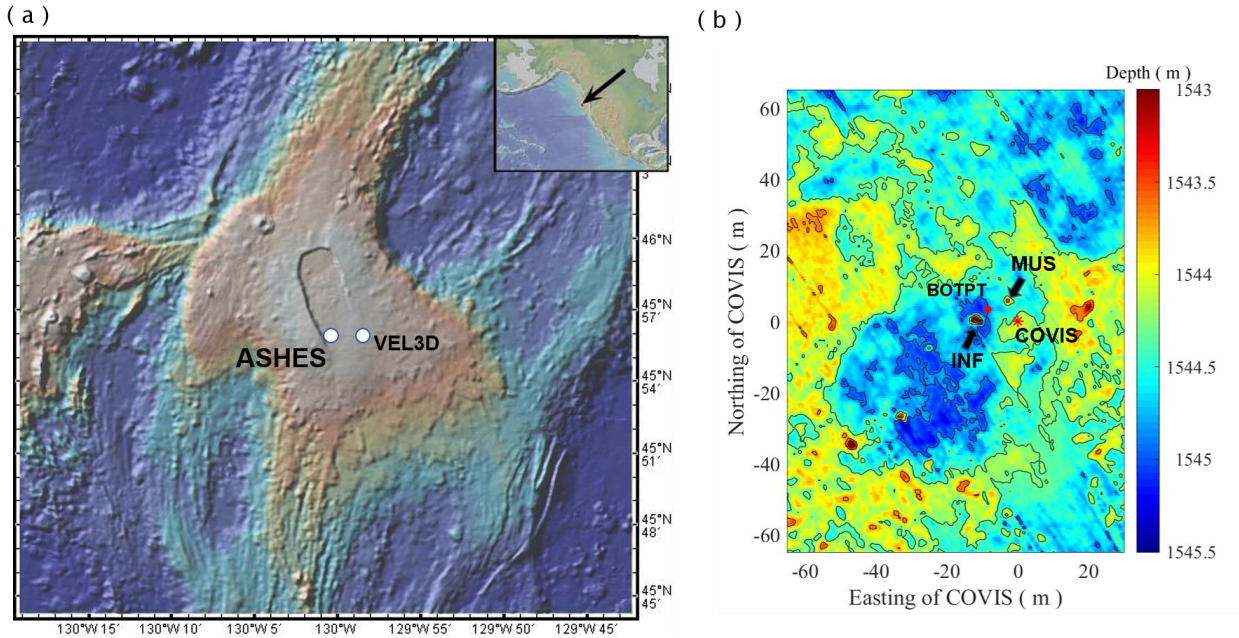

Figure 1: (a) Bathymetry of Axial Seamount. The white dots mark the locations of ASHES hydrothermal vent field and the 3D single point velocity meter (VEL3D) deployed in the International District vent field. (b) Bathymetry of the most hydrothermally active region in ASHES vent field. The black arrows point to the locations of the Inferno (INF) and Mushroom (MUS) vents. The red dot denotes the location of the bottom pressure and tilt meter (BOTPT) deployed in ASHES. The red star marks the location of COVIS, which is the coordinate origin (0,0).

Observations of hydrothermal flows for the northern part of ASHES were reported in previous studies. Rona and Trivett (1992) conducted a thermal survey over a 100 by 100 m area enclosing the depression region using a remotely operated vehicle (ROV) carrying a 1-m long vertical thermistor array. They estimated the heat output from both focused and diffuse flow sources to be 2.4-6.4 MW and 15-75 MW respectively from in-situ temperature measurements, which suggested diffuse flow venting was the dominant hydrothermal heat source at ASHES. Pruis and Johnson (2004) measured the flow rate and temperature of the discharge from a diffuse-flow source in ASHES using a fluid sampler cemented to the seafloor. They estimated a volume flux of 48 m^3/yr and a heat flux of 260 W/m^2 for the 1 m^2 area sealed by the sampler. Their measurements also indicate that the vent flow is overpressured and driven predominately by a significant subsurface pressure gradient as opposed to thermal buoyancy. Most recently, Mittelstaedt et al., (2016) measured heat flux of diffuse flow venting from a narrow fracture near the southern end of the depression region using the Diffuse Effluent Measurement System (DEMS), which is a camera system augmented with thermistors that can measure the flow rate and temperature of diffuse-flow effluents. They obtained an estimated heat flux of the crack: 0.07-0.51 MW/m^2, which was subsequently extrapolated over all the cracks detected in a photomosaic survey to get a total heat flux from venting fractures of 0.1-4 MW.

3. Method

3.1 Sonar Configuration and Data Collection

COVIS is an innovative sonar system designed specifically for long-term, quantitative monitoring of hydrothermal flows. The system consists of a modified Reson 7125 SeaBat multibeam sonar mounted on a novel tri-axial rotator at the top of a 4.2-m tower. The electronics and data-handling hardware are contained in a pressure vessel near the base of the tower (Figure 2). The source and receiver transducers on COVIS operate at two frequencies: 400 and 200 kHz. At 400 kHz, the system operates in the 'Imaging' and 'Doppler' modes to acquire water-column backscatter data for imaging focused hydrothermal flows and estimating their vertical velocity and fluxes respectively. At 200 kHz, COVIS operates in the 'Diffuse' mode to acquire acoustic backscatter from the seafloor covered by diffuse hydrothermal discharge. This study focuses on the data recorded in the Imaging and Diffuse modes, and the Doppler-mode data is left to future research.

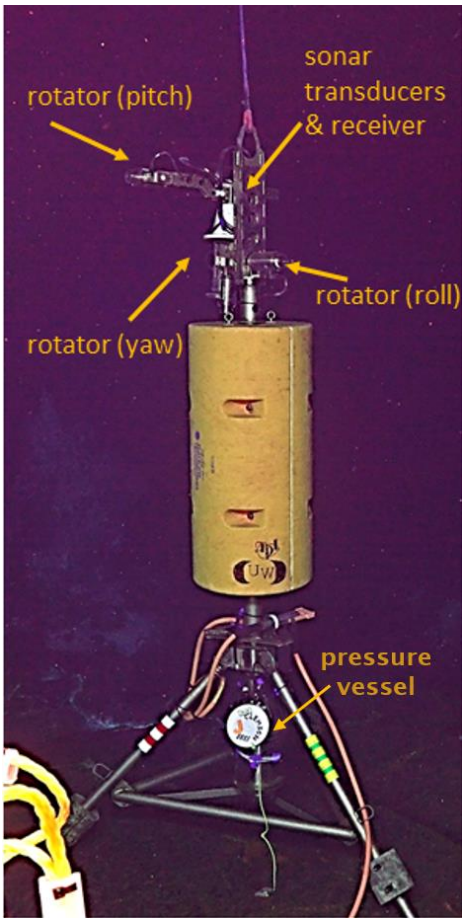

Figure 2: A photo of COVIS taken after its deployment at ASHES vent field. The locations of sonar transducers and receiver along with the three components (pitch, roll, and yaw) of the tri-axial rotator are labeled.

When operating in the Imaging mode (Figure 3a), COVIS employs the 400 kHz source transducer with a transmit beam that is narrow in the elevation coordinate (1° 3-dB beamwidth in the vertical plane) and wide in the azimuthal coordinate (130° 3-dB beamwidth). The receiver array, with digital beamforming, provides 256 0.5º azimuth-wide beams. When collecting an Imaging sweep (we hereafter use the term "sweep" to denote the complete set of pings required to carry out an acoustic measurement), the sonar head pitches upward from -8° to +62° from horizontal in 1° increments. At each step, the source transducer transmits 6 acoustic pulses at a ping rate of 2 Hz. When operating in the Diffuse mode, COVIS employs the 200 kHz source transducer with a transmit beam that covers a wide azimuthal sector (130° 3-dB beamwidth) and has 20° 3-dB beamwidth in elevation. Beamforming on the receiver array provides 128 beams of 1° width (in azimuth). When collecting a Diffuse sweep (Figure 3b,c), the sonar head is pitched downward at 20° below horizontal, and the source transducer transmits 40 acoustic pulses at a ping rate of 2 Hz. To expand the areal coverage in the azimuthal coordinate, during a regular scanning cycle in Diffuse mode, the sonar pans successively to align the receiver's central beam with three nominal headings (relative to true north): 289°, 224°, 4° and collect a sweep of seafloor backscatter data from each 128°-wide sector (Figure 4). In both modes, the backscatter signals received are demodulated, and the resulting complex waveforms are compressed and stored temporarily on COVIS's local hard drive before being transferred to

the OOI's database on land through the fiber-optic cables of the observatory. The data collection and onboard processing combined take approximately 15 min for an Imaging sweep and 2 min for a Diffuse sweep. When operating at full capacity, COVIS records one Imaging sweep and a set of three Diffuse sweeps at the three headings on an hourly basis.

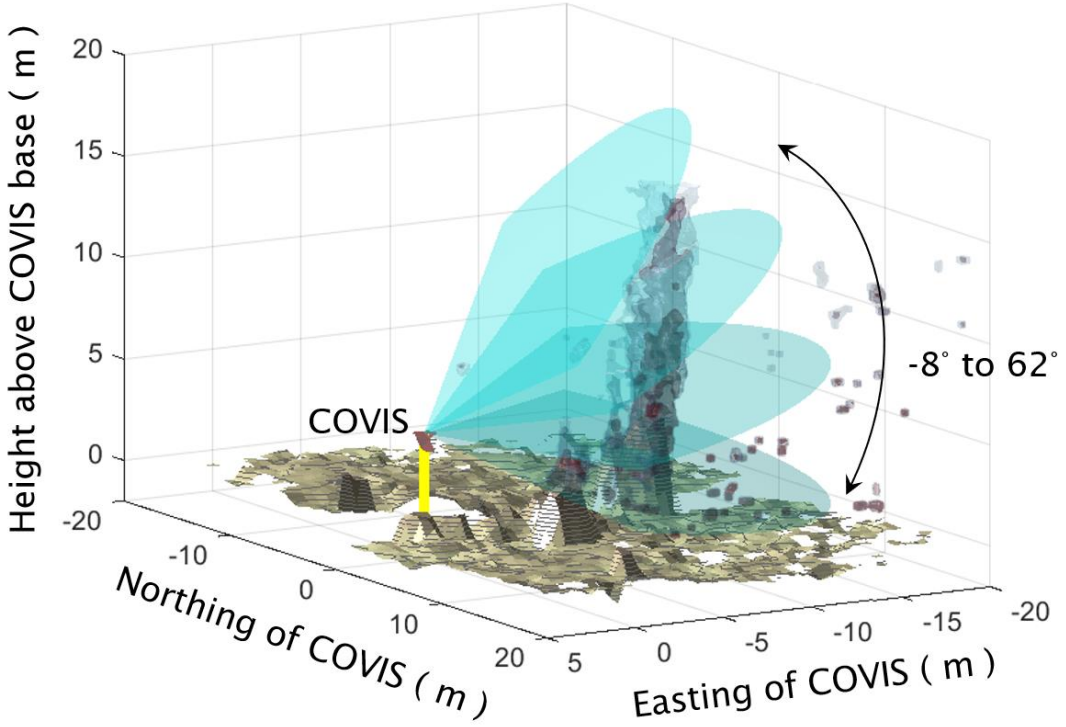

Figure 3: Schematic of acoustic data collection in the Imaging mode of COVIS, in which the sonar head pitches upward from -8° to +62° from horizontal in 1° increments. The background shows the seafloor topography generated from a sweep of special Imaging-mode data recorded following the deployment (see Appendix) overlaid by a plume image generated from a regular Imaging-mode sweep (Section 3.2).

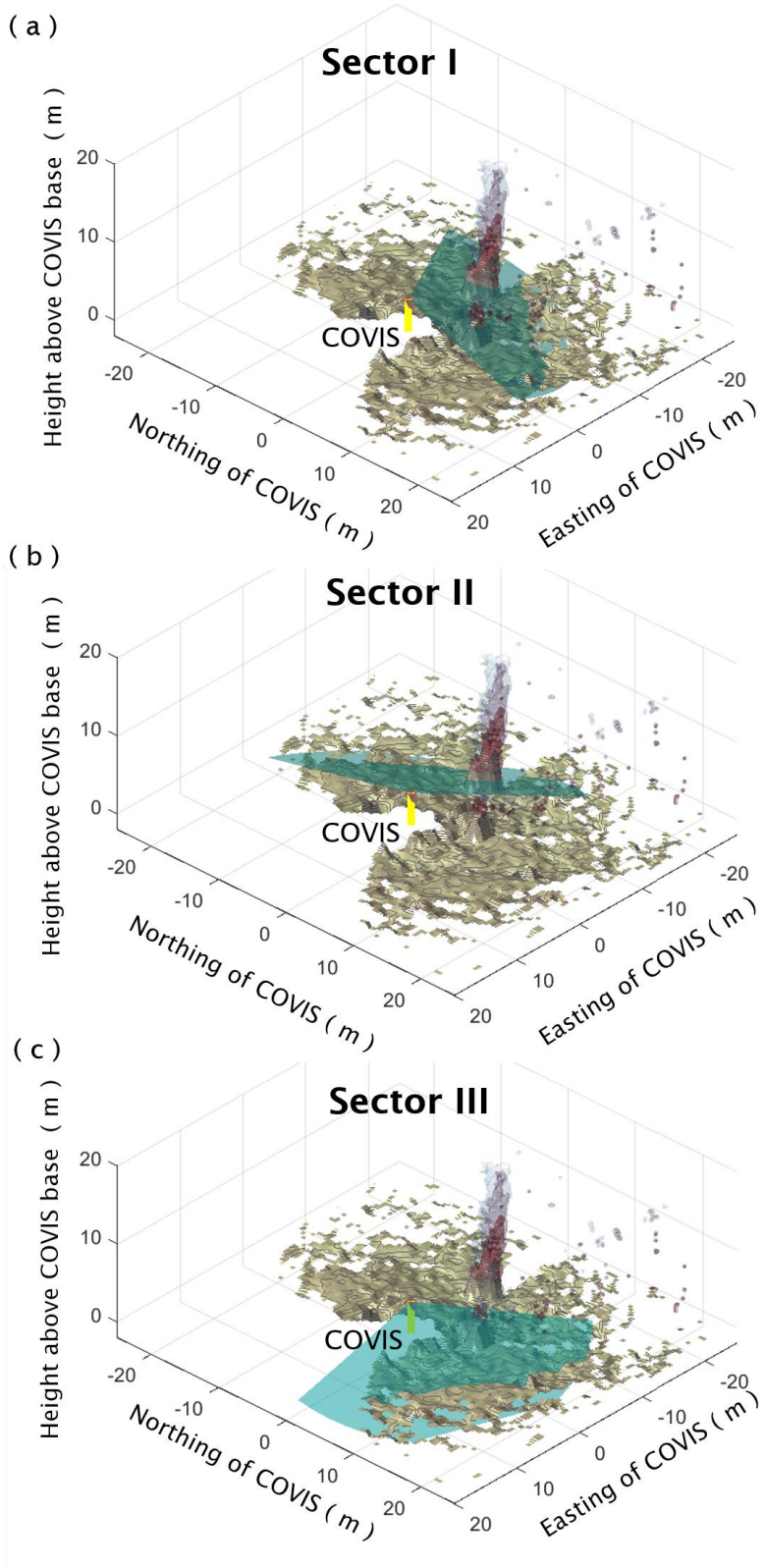

Figure 4: Schematic of acoustic data collection in the Diffuse mode of COVIS, in which the sonar pans successively to align the receiver's central beam with three nominal headings (relative to true north): 305° (a), 240° (b), 20° (c) and record seafloor backscatter from three 128°-wide sectors respectively. The background is the same seafloor topography and plume image as in Figure 3.

205

206

3.2 Focused Flow Imaging

After downloading the raw data recorded in the Imaging mode from the OOI database, we follow the procedures described below to generate 3D images of focused hydrothermal flows (Figure 5). 1) We align the phases of the successive backscatter time series recorded at each elevation step in a sweep by matching the corresponding digitized replicas of the transmitted signal logged in the receiver's monitor channel. Doing so eliminates the artificial ping-to-ping phase variation due to the time jitter between the instant of transmission and beginning of digitization. 2) We band-pass filter the phase-corrected backscatter time series to remove noise outside the nominal bandwidth (three times the inverse of pulse width). 3) We conduct digital beamforming to map the backscatter onto range-azimuth coordinates. 4) We take the differences between consecutive pings received at a given elevation step and then average the results. Doing so removes the backscatter from fixed objects (e.g., a sulfide structure), which are expected to be constant between consecutive pings, while preserving the backscatter from the water column. 5) We remove the sidelobe returns using the OS-CFAR method (de Moustier, 2013). In addition, we remove ambient noise by masking out backscatter with low signal-to-noise ratios relative to a noise floor measured on-site when the sonar was pointed at an 'empty' water column without apparent hydrothermal flows. 6) We calibrate the backscatter time series to obtain volume backscattering coefficient (s_v) (i.e., backscattering cross-section per unit volume per unit solid angle in units m^{-1}) by compensating for transmission loss, receiver sensitivity, and transducer beampatterns. 7) We determine the real-world coordinates relative to COVIS's bottom of each backscatter based on the three-dimensional orientation measured by a tilt-compensated compass module (TCM) mounted on the sonar head and the readings from the tri-axial rotator. 8) Finally, we interpolate s_v onto a 3D grid with a uniform spacing of 0.25 m in all three dimensions using a weighted nearest-neighbor method in which the weight function is inversely proportional to the distance between a given data point and the nearest grid point. The gridded data is then visualized to generate a 3D image of the plumes rising from the major sulfide structures, which is then overlaid on the seafloor topography mapped using the special Imaging-mode data recorded following the deployment of COVIS (see Appendix).

3.3 Diffuse Flow Mapping

The processing of the Diffuse-mode data begins with the same phase-correction, filtering, digital beamforming, and ambient noise-removal procedures as described above. Different from imaging a hydrothermal plume based on its backscatter intensity, our analysis of the Diffuse-mode data maps the spatial distribution of hydrothermal sources exploiting the temporal variation of seafloor backscatter pressure p due to the distortion of acoustic waves propagating through the near-bottom thermal anomalies associated with vent fluids.

The normalized variance of pressure amplitude (K_p) is calculated from the following expression

$$K_p = \frac{\langle |p|^2 \rangle}{\langle |p| \rangle^2} - 1 \quad (1)$$

where $\langle \dots \rangle$ denotes the ensemble average over the pings transmitted within a 4-sec period. We then determine the location of each K_p measurement on the seafloor based on the readings from the TCM and rotator along with the seafloor topography mapped following the deployment (see Appendix). Finally, we interpolate K_p onto a 2D grid with a uniform spacing of 0.5 m in both coordinates using the weighted nearest-neighbor method described in Section 3.2. The gridded

result is then visualized to generate diffuse flow maps, where regions with high K_p are considered potential locations of hydrothermal sources (Figure 7).

3.4 Thermal Survey

On July 6, 2018, we conducted a thermal survey to map the near-bottom temperature field over a 40 by 40 m area centered at the Inferno vent within ASHES. The purpose of this survey was to search for a potential deployment location for COVIS and create a thermal map of hydrothermal sources that can later be compared with the acoustic observations. During the survey, ROV Jason flew along nearly zonal track lines separated by 2.5 m at a speed of 0.1 m/s with a 5-m long thermistor array hanging from the vehicle's underside (Figure S1 in the supporting information). The array carries fourteen thermistors, six of which were mounted on a 1-m tall bottom frame in 0.2 m intervals, and the rest were tied on a 4.5-m long string in 0.5 m intervals between the frame and the float. All thermistors (RBRsolo T: https://rbr-global.com/products/compact-loggers/rbrsolo-t) were self-contained, had fast response (time constant ~ 0.1 sec) and high accuracy (~0.002 ℃), and were programed to sample at 4 Hz for the survey. In addition, the topmost and bottommost thermistors were bundled with pressure sensors (RBRduet T.D: https://rbr-global.com/products/compact-loggers/rbrduet-td), whose data were used to determine the depths of each thermistor on the array during the survey. During most of the survey, the ROV flew at a low altitude so that the bottommost thermistor was within 2 m of the seafloor.

4. Results

4.1 Focused Flow Images

The acoustic images generated from COVIS's Imaging-mode data show evidence of focused flows issuing from Inferno and Mushroom vents in the form of rising plumes (Figure 5). Between the two vents, Inferno's plume is much bigger and better defined in the acoustic images, which is consistent with the field observations that Inferno hosts much more vigorous venting than Mushroom. A visual survey of Inferno's summit during the dive on July 6, 2018 revealed vigorous focused discharge from the tops of 6-7 narrow, chimney-like structures and growth of biology at their base and surrounding areas that indicate venting of low-temperature diffuse flows (Figure 6). The discharge from those 'black-smoker' chimneys coalesce within a few meters above the summit into a single plume as reflected in the acoustic image (Figure 7).

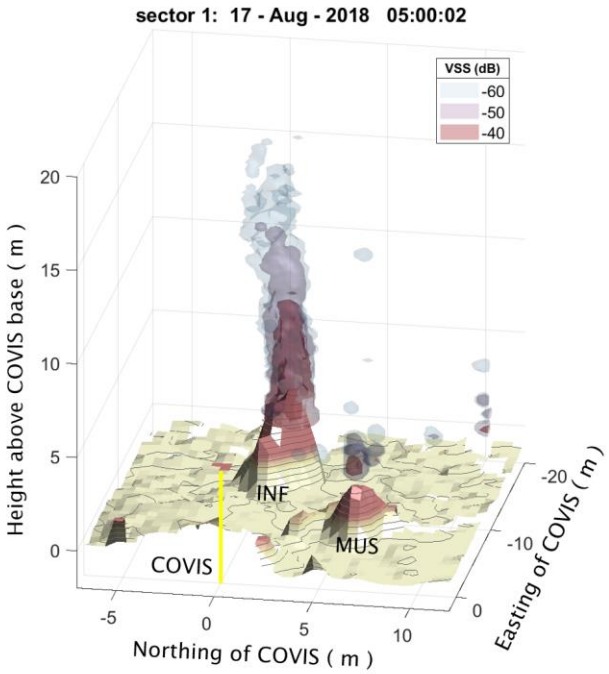

Figure 5: An acoustic image of focused hydrothermal flows generated from an Imaging-mode dataset recorded on Aug 19th, 2018. The Inferno (INF) and Mushroom (MUS) vents are labeled, and the yellow bar denotes COVIS. The color contours correspond to three isosurfaces of backscatter intensity (expressed as volume backscattering strength: $S_v = 10\,log_{10}\,s_v$, where s_v is the volume backscattering coefficient) of -40 dB (red), -50 dB (magenta), -60 dB (blue).

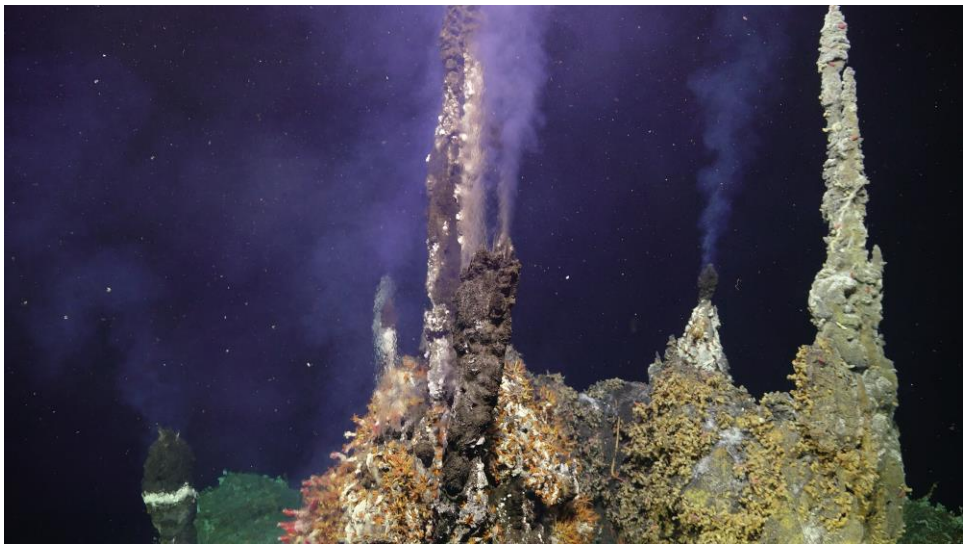

Figure 6: A photo of the summit of Inferno taken using a high-definition camera on ROV Jason following the thermal survey conducted on July 6, 2018. Hydrothermal venting is visible as vigorous focused discharge from the tops of 6-7 narrow, chimney-like structures. The growth of biology at the base of those chimneys indicates venting of low-temperature, diffuse flows in those areas.

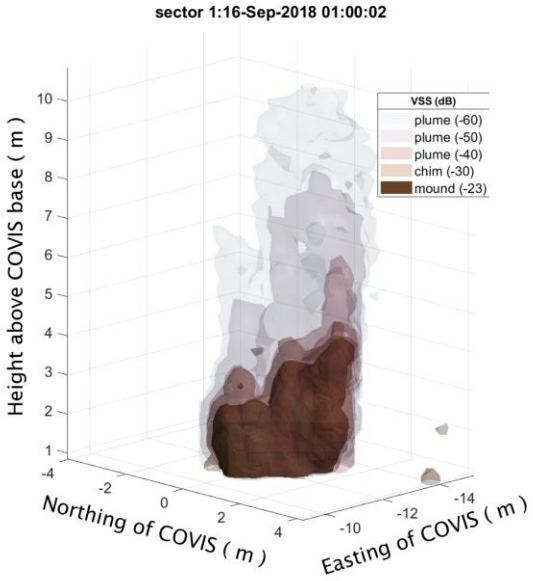

297 *Figure 7: A close-up of chimneys and merging plumes above Inferno.*

298 In a series of images generated from the data recorded in August 2018, the height of the
299 Inferno plume varies with time and the plume axis bends, presumably, towards the downstream
300 directions of local currents (see Animation S1 in the supporting information). As the number of
301 images of the plume above Inferno Vent collected increases, the extent of the variability of the
302 plume appearance becomes evident (Figure 8). Plumes vary between simple rising (buoyant)
303 columns to complex fingering to short horizontal plumes. Sometimes there doesn't even seem to
304 be a plume evident in the acoustic image.

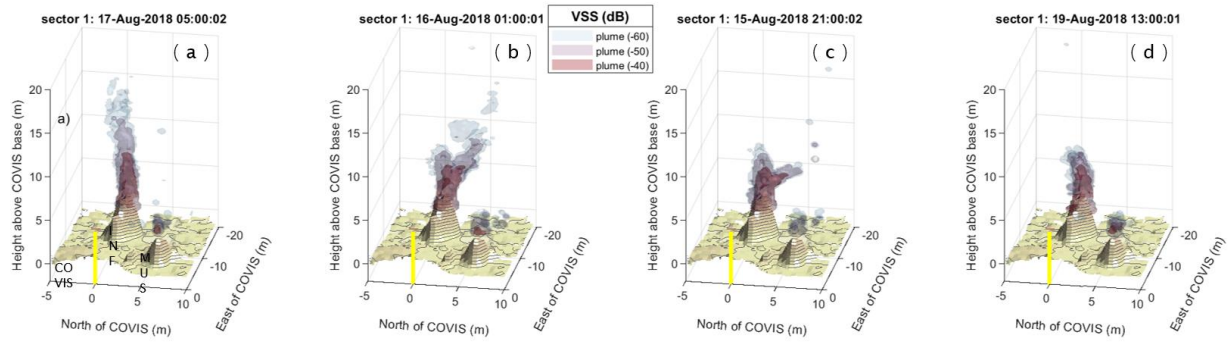

305 *Figure 8. Four selected images from the COVIS Imaging time series during August 2018 are*
306 *shown to illustrate the variability of Inferno Vent's plume. Variations in the Mushroom Vent's*
307 *plume are visible as well although not as dramatic. Plumes above Inferno Vent vary from (a)*
308 *simple rising column to (b) complex fingering to (c) horizontal plume branches to (d) no obvious*
309 *plume above 10 m above bottom. Dynamically, the isosurfaces corresponding to weaker (lower)*
310 *signal levels should have longer extents along the centerline path of the plume (but not*
311 *necessarily greater vertical extent). This holds for (a), (b), and to a lesser extent (c), but not for*
312 *(d).*

The lowest value isosurface shown (-60 dB) defines the apparent height of the plume and the apparent length of the centerline (Figure 9). However, the actual detected plume may continue beyond the shown isosurfaces. Dilution during plume rise due to mixing with ambient seawater results in a weakening signal strength along the plume centerline (hence the isosurface boundaries cross the centerline in Figures 5-9). The apparent rate of dilution can be estimated based on distance along the centerline between isosurface outlines. The visible changes in the apparent length of the centerline and the apparent rate of dilution along the centerline (distance of contour spacing along centerline) suggest changes in dilution rate. Moderately bent plumes show increased dilution rates (closer contours along centerlines) relatively to more vertical plumes, which is likely a result of forced entrainment by ambient currents that leads to enhanced mixing. Highly bent (near horizontal) plumes are observed only in conjunction with a short vertical apparent plume.

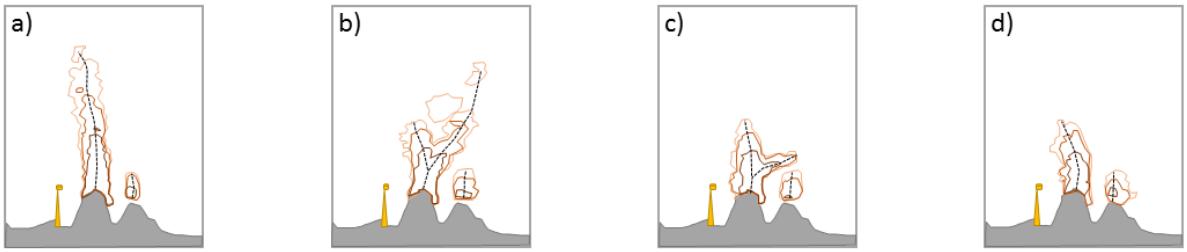

Figure 9. Interpretations of the COVIS Imaging examples are presented to clarify the hydrodynamic structure observed. Solid orange lines show the isosurface outlines (dark=-40 dB; medium=-50 dB; light =-60 dB) while dashed black lines show the centerlines. A solid block gives a rough sense of the topography of the sulfide mounds and lava flow surfaces. A yellow triangle topped with a cylinder shows COVIS's location and the height of the sonar head. Examples are in the same order from the same data as Figure 8.

4.2 Diffuse-flow Maps

The maps of normalized amplitude variance (K_p) generated from the Diffuse-mode data indicate that diffuse discharge is primarily concentrated in areas near Inferno and Mushroom and within three 'hotspot' regions labeled 'H1', 'H2', and 'H3' in Figure 10. In order to validate the use of K_p as an indicator for diffuse-flow discharge, we compare the K_p map with the map of near-bottom temperature measured during the thermal survey conducted before COVIS's deployment (Figure 11a). Overall, most of the 'hotspots' on the thermal map that are within COVIS's field-of-view overlap, at least partially, with regions of high K_p (Figure 11b). The region that has relatively high temperatures but small K_p to the southeast of COVIS is outside the sonar's field-of-view. On the other hand, the areas trailing behind Mushroom and hotspot H3 appear to have large Kp but no significant temperature anomaly. Such mismatch is likely due to the distortion of acoustic signals passing through the plumes issuing from Mushroom and a focused source in H3 (Figure 11c) as opposed to diffuse flows on the seafloor. In other words,

those areas are in the plumes' 'shadows' and do not necessarily have significant diffuse-flow activity. A telltale sign that those regions are in the plumes' shadows is that the outer edges of those regions are approximately in line with the acoustic lines-of-sight (Figure 11b). Outside those shadows, the spatial correspondence between K_p and bottom-temperature is reasonably good given that the in-situ and acoustic measurements were conducted more than three weeks apart and there is a 1-2 m uncertainty in the locations of both measurements due to the inaccuracy of the ROV's navigation information and COVIS's compass reading.

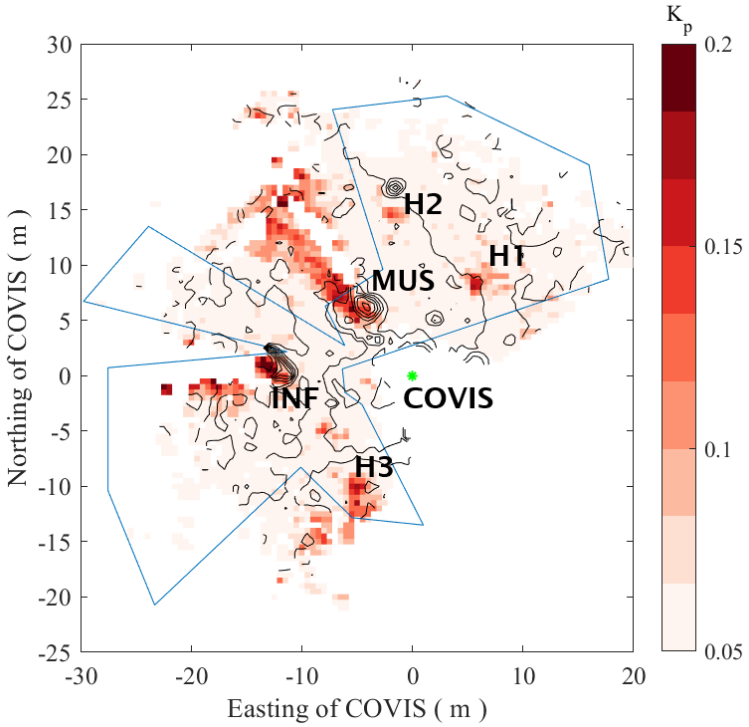

Figure 10: A composite map of normalized backscatter amplitude variance (K_p) generated from the Diffuse-mode data recorded on Aug 19th, 2018. This map is created by merging and interpolating a total of 36 sweeps recorded at the three nominal headings (289°, 224°, 4°) during the day onto the 2D grid using the weighted nearest-neighbor method. The black contours denote seafloor topography measured by COVIS (see Appendix) in 0.5 m intervals. The locations of Inferno (INF) and Mushroom (MUS) vents are labeled, and the green dot marks COVIS's location (0,0). The three 'hotspot' regions discussed in the text are labeled 'H1', 'H2', and 'H3'. The blue polygon demarcates the area included in the diffuse-flow areal extent estimation discussed below.

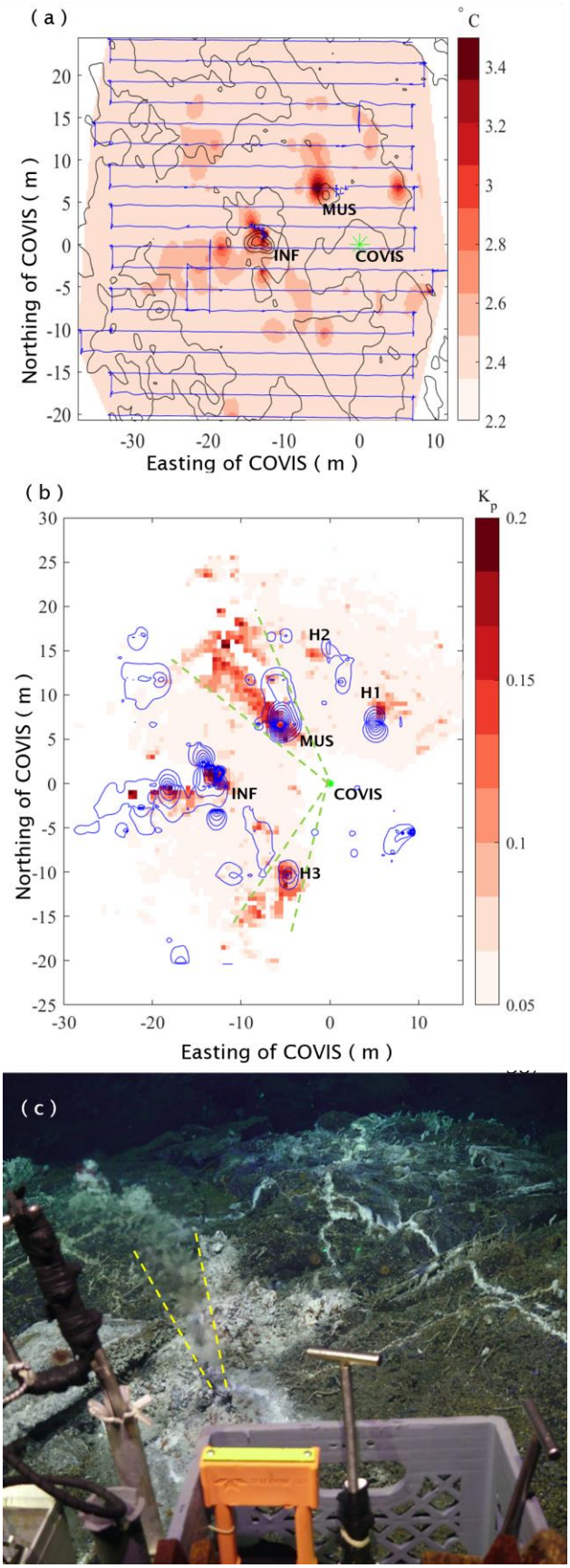

Figure 11: (a) Map of near-bottom temperature recorded by the bottom-most thermistor on the array during the thermal survey conducted before COVIS's deployment. Survey tracklines (blue) and bathymetric contours (black, 0.5-m intervals, data courtesy of OOI) are overlaid. The locations of Inferno (INF) and Mushroom (MUS) are labeled. The green star marks the location of COVIS (0,0). (b) Near-bottom isotherms (blue, 0.1°C intervals) overlaid on the K_p *map shown in Figure 10. The green dashed lines are the seafloor projections of COVIS's acoustic lines-of-sight that align with the outer edges of the 'shadows' cast by the plumes from Mushroom and hotspot H3. (c) An image taken during the dive on July 30th, 2018 that shows a mostly clear, shimmering plume issuing from a focused source located at hotspot H3. The yellow dashed lines mark the approximate lateral boundaries of the plume visible in the image.*

The series of diffuse-flow maps generated from the data recorded in Aug-Sept 2018 show considerable spatial and temporal variations (see Animations S2, S3, and S4 in the supporting information). To investigate those variations, we estimate the areal extent of diffuse-flow within the sonar's field-of-view that is arbitrarily determined as where K_p>0.15 inside a polygon that masks out the artifacts in the shadows of the plumes from Mushroom and hotpot H3 (Figure 10). In Sector 1, which hosts the most vigorous venting among all sectors, the diffuse-flow area shows substantial fluctuations over the approximately two-month period following the deployment of COVIS in 2018 (Figure 12a). Upon closer inspection, those fluctuations are mostly periodic, whose periodogram has significant peaks at tidal (semi-diurnal ~ 0.5 day; diurnal ~ 1 day), near-inertial (~0.65 day), and 0.26-day periods. In addition, there are significant peaks around longer periods of 1.3, 2.4, and 4.3 days (Figure 12b). On the other hand, the total diffuse flow area within the sonar's full field-of-view shows no apparent long-term trend or episodic changes, which indicates the venting activity in ASHES is relatively steady during the measurement period (Figure 13).

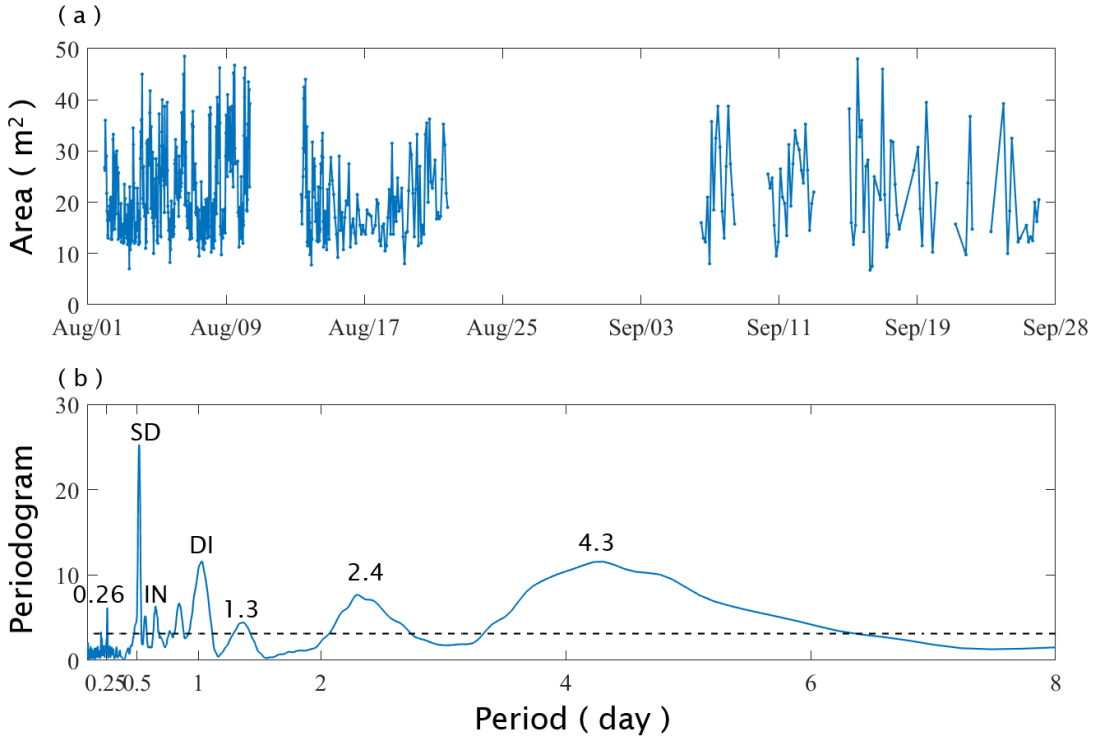

Figure 12: Time series (a) and periodogram (b) of diffuse-flow areal extent in Sector I. The gaps in the time series reflect stoppage of data collection due to observatory power outage and adjustment of sonar operation. The data collection also became irregular with a reduced average sampling rate in Sept 2018 because of an internal issue of the sonar when switching between Imaging and Diffuse modes. The horizontal dashed line denotes the 5% significance level. The noticeable peaks in the periodogram and their periods are labeled (SD: semi-diurnal, DI: diurnal, IN: inertial). The periodogram was calculated using a modified Lomb-Scargle method for unevenly spaced time series (Pardo-Igúzquiza and Rodríguez-Tovar 2012).

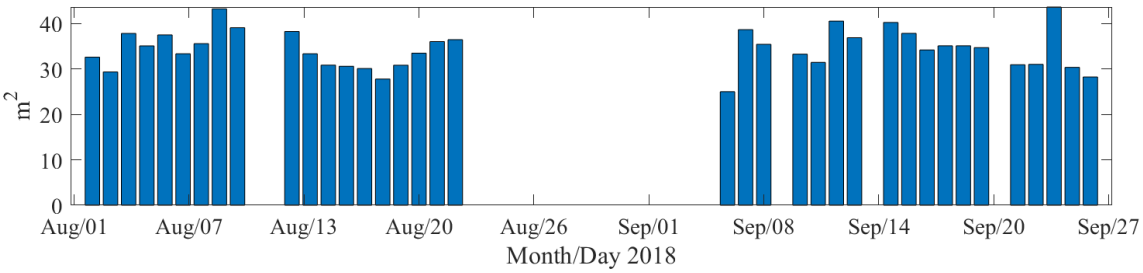

Figure 13: Time series of daily averaged diffuse-flow areal extent within COVIS's full field-of-view. The daily average is first taken for each sector and then combined in such a way that the contributions from the regions where Sector 1 overlaps with Sectors 2 and 3 are subtracted from the total daily averages for those two sectors before adding to that for Sector 1.

5. Discussion

5.1 Drivers for variations in plume appearance

Possible explanations for variations in plume appearance include difficulties imaging weak or horizontal plumes, variable bottom currents, variable discharge rates, and variable fluid composition. Variations in bottom current direction and speed almost certainly account for most of the observed variations, particularly changes in the direction and extent of bending of the plume. However, variations in discharge rate could also result in variations in bending (without a changing current) of the plume and its thermal anomalies that lead to variations in backscatter intensity.

Increased dilution rates (closer contours along centerlines) in bent plumes are likely due to the forced entrainment expected from interactions with currents (Xu et al., 2013; Rona et al., 2006). If the acoustic signal from the plume fades out at -60 dB (due to low signal-to-noise ratio), then the increased dilution for highly bent plumes would explain a shorter centerline extent but not the conjunction of a near horizontal plume and short vertical plume. Vortex splitting (Crabb et al., 1981) could result from interactions with strong currents, producing the appearance of complex fingering. Alternatively, multiple sources may result in independent plumes of differing rise and bending rates, which the acoustic data may not fully resolve (given the 0.25 – 0.50 footprint of the 1° acoustic beam).

Explaining the very short vertical plumes, whether or not in conjunction with near horizontal plumes, is challenging. Most of the short vertical plumes show signs of a near horizontal plume; for those that do not, it is possible that occlusion by the Inferno sulfide mound limits COVIS's ability to see small horizontal plumes. An interesting possible explanation for no apparent or very short plumes would be a collapsing plume. High salinity fluids (brines) could initially rise due to buoyancy but lose that buoyancy with dilution causing them to fall back down (collapse) [Turner 1966]. This might look like a short stubby plume. But it would imply highly variable discharge salinities.

5.2 Effects of Ocean Tides and Currents on Diffuse Discharge

The acoustically estimated diffuse-flow areal extent shows significant periodic variations at tidal and non-tidal frequencies (Figure 12b). In general, those periodic oscillations in hydrothermal discharge can originate from two major sources. First, the poroelastic response of crustal fluids to varying seafloor pressure (e.g., tidal loading) leads to oscillations of the vertical pore pressure gradient in the subsurface, which then drives time-delayed oscillations in exit flow rates and hence thermal fluxes of hydrothermal discharge (Xu et al., 2017). Second, near-bottom currents can enhance the mixing of hydrothermal effluent with ambient seawater, which reduces the thickness of the thermal boundary layer created by diffuse venting on the seafloor and hence the acoustically estimated diffuse-flow area. Third, near-bottom currents can cause bending of focused plumes in directions that transect acoustic lines-of-sight. This could produce artificial acoustic anomalies in regions outside the 'shadow' zones delimited in Figure 11b and hence an increase in acoustically estimated diffuse-flow area. Based on the in-situ temperature measurements made at the Lucky Strike Hydrothermal Field on the Mid-Atlantic Ridge, Barreyre et al., (2014) suggested that diffuse flows are mostly affected by bottom currents while focused flows are mostly affected by tidal loading. Mittelstaedt et al., (2016) observed tidal variations in the velocity and temperature of diffuse discharge from a fractured network at ASHES, which were attributed to the combined effects of tidal pressure and bottom currents.

To determine the relative importance of pressure- and current-driven processes in driving the oscillations in diffuse-flow area, we examined the bottom current and pressure data recorded by a 3D single-point velocity meter (VEL3D) deployed at the International District hydrothermal vent field on the southeastern side of Axial's caldera (Figure 1a) and a bottom pressure and tilt meter (BOTPT) deployed at ASHES (Figure 1b). While the variations in pressure are primarily modulated by tides (Figure 14a), significant non-tidal oscillations exist in bottom current velocity, especially its clockwise rotating component, at the inertial, 0.26-day, 1.3-day, and longer periods between 2 and 5 days (Figure 14b). Previous field observations and numerical simulations have shown the presence of inertial and 3- to 6-day (the 'weather' band) oscillations in the bottom currents near Axial and other parts of the Juan de Fuca Ridge (Cannon et al., 1991; Cannon & Thomson 1996; Xu et al., 2013, Xu et al., 2017). Xu et al., (2013) interpret the inertial oscillations in bottom currents as a result of the downward propagation of the surface wind-driven inertial waves. Although the exact generation-mechanism for the weather-band oscillations is uncertain, previous studies have shown evidence for local atmospheric forcing (e.g., storms) to be the primary source (Cannon & Thomson 1996). The 0.26-day oscillations in bottom currents can arise from the nonlinear wave-wave interaction of the semi-diurnal constituent with itself, which generates waves at twice the frequency of the semi-diurnal constituent. Similarly, the 2.4-day peak can originate from the nonlinear interaction of the semi-

diurnal constituent with the near inertial oscillations, which generates waves at the frequency that is the difference between those of the two sources.

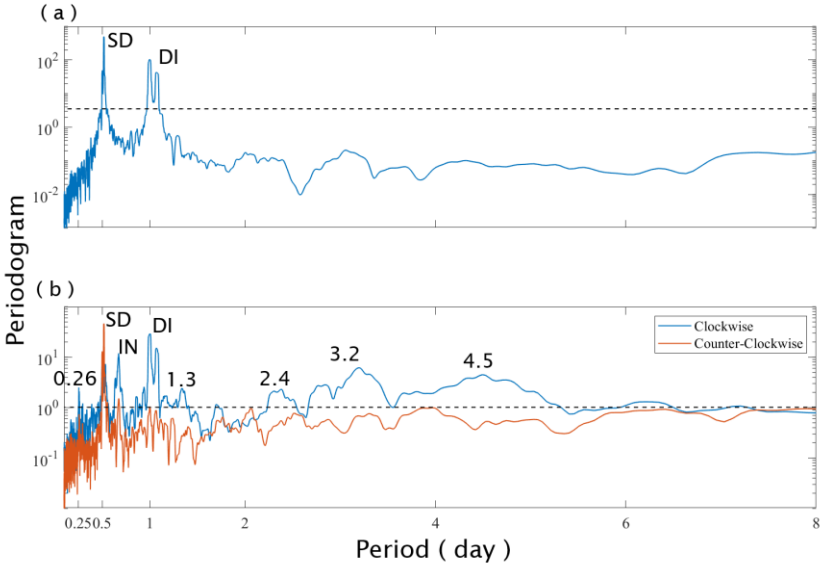

Figure 14: Periodograms of seafloor pressure (a) and bottom current velocity (b) from the data recorded by) BOTPT in ASHES (Figure 1a) and VEL3D in International District (Figure 1b) from July to Dec 2018 respectively. The periodogram of the velocity vector is decomposed into clockwise (red) and counterclockwise components (blue). The noticeable peaks and their periods are labeled (SD: semi-diurnal, DI: diurnal, IN: inertial). The horizontal dash lines denote the 1% significance level. The periodogram was calculated using a modified Lomb-Scargle method for unevenly spaced time series (Pardo-Igúzquiza and Rodríguez-Tovar 2012).

Comparing the periodograms of diffuse flow areal extent in Sector I with those of pressure and currents suggests that bottom currents are the likely source for the non-tidal (inertial, 4-day, 0.26-day, 1.3-day, 2.4-day and 4.3-day) oscillations in diffuse-flow area since significant variations at the same or similar periods are present in bottom currents but not pressure (Figures 12b and 14). On the other hand, we cannot rule out the contribution of seafloor pressure to the tidal variations in diffuse-flow area, which will be further investigated in our future research.

6. Concluding Remarks

The preliminary data products presented in this paper have demonstrated COVIS's ability to quantitatively monitor hydrothermal discharge with sufficient spatial and temporal coverage to provide the research community with key observational data for studying the linkage of hydrothermal activity with oceanic and geological processes during the dynamic period leading up to the next eruption of Axial. The acoustically estimated diffuse-flow areal extent shows no

long-term trend or episodic changes but significant periodic oscillations at tidal and non-tidal frequencies. This points to relatively steady-state venting in ASHES that is modulated by bottom currents and potentially seafloor pressure during the initial two months of COVIS's deployment. Unfortunately, a broken cable on the sonar platform had caused the regular data-collection routine to suspend after Sept 2018. We recovered COVIS in June 2019 and replaced the broken cable before redeploying the sonar platform in July 2019. The data collection has been ongoing since then, while the processing and analysis of the new data is currently underway. Extension of the treatment of backscatter data to enable more quantitative assessment of thermal activity would be highly desirable. For example, a model that would allow estimation of temperature statistics could be evaluated by comparison of acoustically derived results with in-situ thermistor data.

7. Acknowledgements

The COVIS and thermistor-array data presented in this paper will be available on an OOI-hosted FTP site that is expected to be launched in summer 2020. The bathymetric data for the ASHES vent field can be downloaded from Marine Geoscience Data System (MGDS) (http://www.marine-geo.org/index.php). The current-meter and bottom pressure recorder data used in this work are accessible through the OOI's data portal (https://ooinet.oceanobservatories.org/). The authors gratefully acknowledge support from the National Science Foundation. We appreciate the operation support from the OOI team at University of Washington and Rutgers University. We are also thankful to the ROV Jason team, captains and crews of R/V Roger Revelle and R/V Thomas G. Thompson, and the engineering team at APL-UW led by Tim McGinnis for their support for sonar preparation, at-sea experiments, and distribution of COVIS data.

Appendix: Bathymetric data collection by COVIS

In order to map the seafloor topography within COVIS's field-of-view, we collected a sweep of special Imaging-mode data at each of the three nominal headings (289°, 224°, 4°) following the deployment of COVIS in 2018. At each heading, the sonar head pitches upward from -56° to 28° from horizontal in 0.5° increments. At each step, the source transducer (400 kHz) transmits two pulses at a ping rate of 5 Hz and the receiver records the backscatter signals following each transmission. The processing of the special Imaging-mode data begins with the same phase-correction, filtering, digital beamforming, and ambient noise-removal procedures described in Section 3.2. The backscatter time series is then calibrated to obtain volume backscattering coefficient (s_v) (i.e., backscattering cross-section per unit area per unit solid angle in units m^{-1}) by compensating for transmission loss, receiver sensitivity, and transducer beampatterns. Subsequently, we locate the backscatter from the seafloor and sulfide structures by finding the maximum s_v in each acoustic beam formed at each pitch angle and determine the corresponding elevation relative to COVIS's bottom based on the readings from the TCM and rotator. Finally, we interpolate the results onto a 2D grid with a uniform spacing of 0.25 m to generate a map of seafloor topography within the sonar's field-of-view (Figure A1).

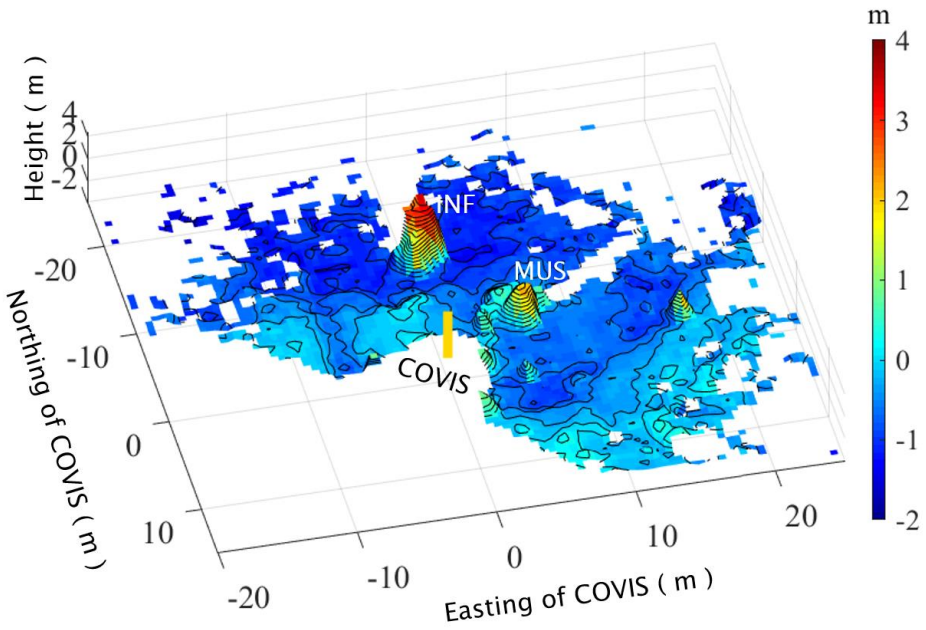

Figure A1: Seafloor topography within COVIS's field-of-view generated using the special Imaging-mode data collected following the deployment in July 2018. The topography is shown as elevation relative to the base of COVIS. The locations of COVIS, Inferno (INF), and Mushroom (MUS) are marked.

References:

Barreyre, T., Escartín, J., Sohn, R.A., Cannat, M., Ballu, V. and Crawford, W.C., 2014. Temporal variability and tidal modulation of hydrothermal exit-fluid temperatures at the Lucky Strike deep-sea vent field, Mid-Atlantic Ridge. *Journal of Geophysical Research: Solid Earth*, *119*(4), pp.2543-2566.

Cannon, G.A., Pashinski, D.J. and Lemon, M.R., 1991. Middepth flow near hydrothermal venting sites on the southern Juan de Fuca Ridge. *Journal of Geophysical Research: Oceans*, *96*(C7), pp.12815-12831.

Cannon, G.A. and Thomson, R.E., 1996. Characteristics of 4-day oscillations trapped by the Juan de Fuca Ridge. *Geophysical research letters*, *23*(13), pp.1613-1616.

Chadwick, W.W., Butterfield, D.A., Embley, R.W., Tunnicliffe, V., Huber, J.A., Nooner, S.L. and Clague, D.A., 2010. SPOTLIGHT 1| Axial Seamount: 45° 57.00'N, 130° 00.00'W. *Oceanography*, *23*(1), pp.38-39.

Chadwick, W. W., Jr., and S. L. Nooner (2019), Forecasting Eruptions Based on an Inflation-Predictable Pattern of Deformation at Axial Seamount, NE Pacific Ocean. Abstract presented at 2019 IUGG General Assembly, Montreal, Canada, 8-18 Jul.

Chadwick, W.W., Paduan, J.B., Clague, D.A., Dreyer, B.M., Merle, S.G., Bobbitt, A.M., Caress, D.W., Philip, B.T., Kelley, D.S. and Nooner, S.L., 2016. Voluminous eruption from a zoned magma body after an increase in supply rate at Axial Seamount. *Geophysical Research Letters*, *43*(23), pp.12-063.

Crabb, D., Dura˜o, D. F. G., and Whitelaw, J. H. (March 1, 1981). "A Round Jet Normal to a Crossflow." ASME. *J. Fluids Eng*. March 1981; 103(1): 142-153. https://doi.org/10.1115/1.3240764

de Moustier, C., 2013, September. OS-CFAR detection of targets in the water column and on the seafloor with a multibeam echosounder. In *2013 OCEANS-San Diego* (pp. 1-2). IEEE.

Embley, R.W., Murphy, K.M. and Fox, C.G., 1990. High-resolution studies of the summit of Axial Volcano. *Journal of Geophysical Research: Solid Earth*, *95*(B8), pp.12785-12812.

Hammond, S.R., 1990. Relationships between lava types, seafloor morphology, and the occurrence of hydrothermal venting in the ASHES vent field of Axial Volcano. *Journal of Geophysical Research: Solid Earth*, *95*(B8), pp.12875-12893.

Jackson, D.R., Ivakin, A.N., Xu, G. and Bemis, K.G., 2017. Sonar observation of diffuse hydrothermal flows. *Earth and Space Science*, *4*(5), pp.230-239.

Kelley, D.S., Delaney, J.R. and Juniper, S.K., 2014. Establishing a new era of submarine volcanic observatories: Cabling Axial Seamount and the Endeavour Segment of the Juan de Fuca Ridge. *Marine Geology*, *352*, pp.426-450.

Mittelstaedt, E., Fornari, D.J., Crone, T.J., Kinsey, J., Kelley, D. and Elend, M., 2016. Diffuse venting at the ASHES hydrothermal field: Heat flux and tidally modulated flow variability derived from in situ time-series measurements. *Geochemistry, Geophysics, Geosystems*, *17*(4), pp.1435-1453.

Palmer, D.R., Rona, P.A. and Mottl, M.J., 1986. Acoustic imaging of high-temperature hydrothermal plumes at seafloor spreading centers. *The Journal of the Acoustical Society of America*, *80*(3), pp.888-898.

Pardo-Igúzquiza, E. and Rodríguez-Tovar, F.J., 2012. Spectral and cross-spectral analysis of uneven time series with the smoothed Lomb–Scargle periodogram and Monte Carlo evaluation of statistical significance. *Computers & geosciences*, *49*, pp.207-216.

Pruis, M.J. and Johnson, H.P., 2004. Tapping into the sub-seafloor: examining diffuse flow and temperature from an active seamount on the Juan de Fuca Ridge. *Earth and Planetary Science Letters*, *217*(3-4), pp.379-388.

Rona, P.A., Palmer, D.R., Jones, C., Chayes, D.A., Czarnecki, M., Carey, E.W. and Guerrero, J.C., 1991. Acoustic imaging of hydrothermal plumes, East Pacific Rise, 21° N, 109° W. *Geophysical Research Letters*, *18*(12), pp.2233-2236.

Rona, P.A. and Trivett, D.A., 1992. Discrete and diffuse heat transfer atashes vent field, Axial Volcano, Juan de Fuca Ridge. *Earth and Planetary Science Letters*, *109*(1-2), pp.57-71.

Smart, C., Roman, C. and Carey, S., 2017. Detection of diffuse seafloor venting using a structured light laser sensor: 1. Development of a classification based detection method. *Earth and Space Science*, *4*(6), pp.348-363.

Caratori Tontini, F., Crone, T.J., de Ronde, C.E., Fornari, D.J., Kinsey, J.C., Mittelstaedt, E. and Tivey, M., 2016. Crustal magnetization and the subseafloor structure of the ASHES vent field, Axial Seamount, Juan de Fuca Ridge: Implications for the investigation of hydrothermal sites. *Geophysical Research Letters*, *43*(12), pp.6205-6211.

Wilcock, W.S., Tolstoy, M., Waldhauser, F., Garcia, C., Tan, Y.J., Bohnenstiehl, D.R., Caplan-Auerbach, J., Dziak, R.P., Arnulf, A.F. and Mann, M.E., 2016. Seismic constraints on caldera dynamics from the 2015 Axial Seamount eruption. *Science*, *354*(6318), pp.1395-1399.

Xu, G. and Di Iorio, D., 2011. The relative effects of particles and turbulence on acoustic scattering from deep-sea hydrothermal vent plumes. *The Journal of the Acoustical Society of America*, *130*(4), pp.1856-1867.

Xu, G., Jackson, D.R. and Bemis, K.G., 2017. The relative effect of particles and turbulence on acoustic scattering from deep sea hydrothermal vent plumes revisited. *The Journal of the Acoustical Society of America*, *141*(3), pp.1446-1458.

Xu, G., Jackson, D.R., Bemis, K.G. and Rona, P.A., 2013. Observations of the volume flux of a seafloor hydrothermal plume using an acoustic imaging sonar. *Geochemistry, Geophysics, Geosystems*, *14*(7), pp.2369-2382.

Xu, G., Jackson, D.R., Bemis, K.G. and Rona, P.A., 2014. Time-series measurement of hydrothermal heat flux at the Grotto mound, Endeavour Segment, Juan de Fuca Ridge. *Earth and Planetary Science Letters*, *404*, pp.220-231.

Xu, G., Larson, B.I., Bemis, K.G. and Lilley, M.D., 2017. A preliminary 1-D model investigation of tidal variations of temperature and chlorinity at the Grotto mound, Endeavour Segment, Juan de Fuca Ridge. *Geochemistry, Geophysics, Geosystems*, *18*(1), pp.75-92.

Xu, G. and Lavelle, J.W., 2017. Circulation, hydrography, and transport over the summit of Axial Seamount, a deep volcano in the Northeast Pacific. *Journal of Geophysical Research: Oceans*, *122*(7), pp.5404-5422.